PAPER

Exploring polynomial based interpolation schemes for photoacoustic tomographic image reconstruction

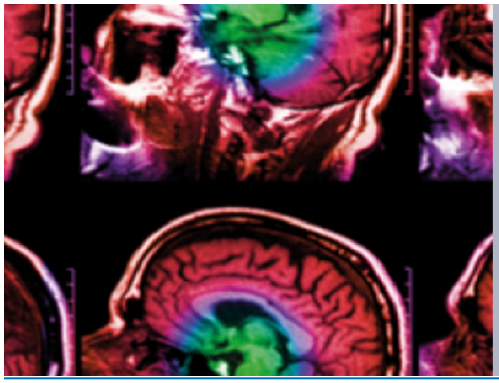

Biomedical Physics & Engineering Express

PAPER

Exploring polynomial based interpolation schemes for photoacoustic tomographic image reconstruction

Avijit Paul, Pankaj Warbal, Amrita Mukherjee, Subhadip Paul and Ratan K Saha

Department of Applied Sciences, Indian Institute of Information Technology Allahabad, Jhalwa, Prayagraj 211015, India

E-mail: ratank.saha@iiita.ac.in

RECEIVED
2 June 2021

REVISED
26 November 2021

ACCEPTED FOR PUBLICATION
3 December 2021

PUBLISHED
13 December 2021

Keywords: nearest neighbor interpolation, bilinear interpolation, bicubic interpolation, biquintic interpolation, photoacoustic image reconstruction

Abstract

Photoacoustic tomography (PAT) imaging employing polynomial-based interpolation methods is discussed. Nearest-neighbor, bilinear, bicubic and biquintic algorithms were implemented for the construction of the model matrix, and images were formed using the Tikhonov regularization and total variation (TV) minimization procedures. The performance of the interpolation methods was assessed by comparing the reconstructed images of three numerical and two experimental phantoms. The numerical and experimental studies demonstrate that the performance of the interpolation schemes is nearly equal for large PA sources. The simplest nearest-neighbor technique provides better image reconstruction for a sparse source compared to the others. The nearest-neighbor protocol may be adopted in practice for vascular imaging using PAT.

1. Introduction

Photoacoustic (PA) imaging is a hybrid imaging modality that uses optical illumination and ultrasound detection [1, 2]. On one hand, the state-of-the-art PA microscopy imaging technique enables to visualization of specialized subunits (organelles) within a cell to individual cells with lateral resolution ranging from hundreds of nanometers to several micrometers. On the other hand, modern PA tomography (PAT) setup can form images of tissue structures located several centimeters deep. A number of reconstruction methods have been developed for this purpose. The goal is to develop a fast and efficient reconstruction algorithm suitable for real-time imaging. Analytical approaches such as universal backprojection algorithm and time-reversal method are simple and fast but they lack to provide quantitative information of the imaging region [3, 4]. In order to overcome this limitation, the model matrix inversion technique has been implemented [5, 6]. In general, this approach is computationally expensive in terms of memory and execution time, however, capable of providing accurate quantitative information of the region of interest. So far, the model matrix has been constructed either by loading spatial impulse response functions of the receivers [5] or by exploring a suitable interpolation scheme such as bilinear interpolation [6].

Image interpolation is of great importance in medical imaging and is often required to achieve various ends [7]. It is a basic tool used for image zooming, shirking, rotating, and performing geometric corrections. Several interpolation kernels with finite sizes have been introduced. Examples include truncated and windowed sinc, nearest neighbor, linear, cubic, quadratic, quintic, Lagrange and Gaussian interpolations [7]. As stated above, PAT image reconstruction was carried out using the bilinear interpolation protocol. To the best of our knowledge, no other polynomial-based interpolation techniques have been deployed so far.

A natural question is how other polynomial-based interpolation algorithms would work in PAT image reconstruction. An attempt has been made in this work to address this issue through simulations. The main contributions of this work are to- (i) present an algorithm for computing the interpolation weights, (ii) implement the nearest-neighbor (NN), bilinear (BL), bicubic (BC), and biquintic (BQ) procedures for the construction of model matrix and (iii) compare the performance of the interpolation techniques for PAT image reconstruction. Regularized solutions have been obtained by deploying the Tikhonov regularization and the total variation (TV) minimization approaches. Image reconstruction has been performed for three

numerical phantoms, namely, Gaussian discs, Derenzo, and vasculature phantoms. PAT experiments have also been conducted with two simple phantoms (a plastic tube containing black ink and a triangular source formed using Graphaite pencil leads). Some standard image quality parameters have been computed for quantitative assessment of the interpolation algorithms. It has been found (via numerical and experimental investigations) that the interpolation schemes produce comparable reconstructed images for a large PA source (disc). Nevertheless, NN may be preferred over higher order interpolations for the formation of a light-absorbing structure with many fine branches (vasculature).

The layout of the paper is as follows. The next section discusses the theoretical foundation of this work. The computational and experimental methods are described in section 3. Section 4 highlights various results obtained in this study. The discussion and conclusions of this work are presented in section 5.

2. Theoretical ingredients

2.1. Reconstruction algorithms

The PAT image reconstruction can be treated as a linear inverse problem which provides a system of linear equations [5],

$$\Lambda z = p_f, \quad \Lambda \in \mathbb{R}^{m\times n}, \quad z \in \mathbb{R}^n, \quad p_f \in \mathbb{R}^m \quad (1)$$

where Λ is the model matrix (or system matrix); z is the unknown representing a spatial map of initial pressure rise/light absorption function; p_f is the measured pressure data. The subscript f stands for an ambient fluid medium where measurement has been carried out.

The model matrix in general depends upon the geometry of the PAT system, speed of sound in the medium, and properties of the individual detectors (e.g., frequency response and sensitivity profile of the receiving aperture). It is generally a large and ill-conditioned matrix. The computation of a reliable solution to equation (1) can be accomplished using the Tikhonov regularization method by minimizing the following cost function [5],

$$\Omega = \|\Lambda z - p_f\|_2^2 + \lambda^2\|Lz\|_2^2, \quad (2)$$

where $\|\cdot\|_\iota$ is the l_ι norm. The quantity λ is the regularization parameter and L is the regularization matrix (a derivative operator); λ and L together control smoothness of the solution.

The standard form of equation (2) has been explored extensively for PAT image generation [i.e., $L = I$ where I is the identity matrix]. For this case, an analytical solution can be obtained, by minimizing equation (2), as,

$$z_r = (\Lambda^T\Lambda + \lambda^2 I)^{-1}\Lambda^T p_f, \quad (3)$$

where T denotes the transpose operator. Further manipulation of equation (3) can be carried out in order to yield a simple expression. For example, the singular value decomposition (SVD) of Λ can be written as,

$$\Lambda = USV^T = \sum_{i=1}^{n} u_i\sigma_i v_i^T, \quad (4)$$

where $V = (v_1, v_2,\ldots,v_n)$, $U = (u_1, u_2,\ldots,u_n)$ are the right and left orthogonal matrices, respectively providing $U^TU = V^TV = I_n$ and $m \geqslant n$; $S = \mathrm{diag}(\sigma_1, \sigma_2,\ldots,\sigma_n)$. The diagonal elements are non-negative and ordered in the descending manner such that,

$$\sigma_1 \geqslant \sigma_2 \geqslant \ldots. \geqslant \sigma_n. \quad (5)$$

The substitution of equations (4) into (3) provides,

$$\begin{aligned} z_r &= (VS^TSV^T + \lambda^2 I)^{-1}VS^TU^Tp_f \\ &= V(S^TS + \lambda^2)^{-1}S^TU^Tp_f \\ &= \textstyle\sum_{i=1}^{n} \dfrac{\sigma_i(u_i^T p_f)}{\sigma_i^2 + \lambda^2}v_i, \end{aligned} \quad (6)$$

where $\frac{\sigma_i}{\sigma_i^2+\lambda^2}$ is the filter factor. The filter factors suppress the contributions from the small singular values, nevertheless, do not impact those of large singular values. It may be emphasized that at higher regularization, the image becomes over smoothed. Small λ values amplify noise in the PA image. There exist several algorithms to find out the optimal value of λ. For instance, L-curve, generalized cross-validation (GCV) methods can be utilized to accomplish this [8, 9].

Another approach called the TV minimization has also been applied for the same purpose. This approach works well for limited view data set. The cost function in this case becomes,

$$\Omega = \frac{\eta}{2}\|\Lambda z - p_f\|_2^2 + \|\nabla z\|_1, \quad (7)$$

where η (>0) is the penalty parameter and ∇ is the gradient operator. The minimization of equation (7) does not offer any analytical solution as in the previous case. Therefore, various computational methods have been developed to obtain numerical solutions. For example, Li *et al* used augmented Lagrangian and alternating direction algorithm (ALADA) for this purpose [10]. In this work, image reconstruction has been performed using the Tikhonov and the TV regularization methods.

2.2. Relationship between initial pressure rise and recorded pressure

The PA pressure data (p_f) in practice are obtained either from experiments or numerical simulations for complex structures. They may also be produced theoretically for simple shapes. The theoretical model that describes the generation and propagation of PA waves for a delta function incident light pulse ($\delta(t)$) is given by [3],

$$\nabla^2 p(\mathbf{r}, t) - \frac{1}{v^2}\frac{\partial^2 p(\mathbf{r}, t)}{\partial t^2} = -\frac{p_0(\mathbf{r})}{v^2}\frac{d\delta(t)}{dt}, \quad (8)$$

where v is the speed of sound in the medium and $p_0(\mathbf{r}) = \Gamma\mu(\mathbf{r})F$ is the initial pressure rise [also defined as z in equation (1)] due to absorption of light with Γ as the Gr ü neisen parameter; $\mu(\mathbf{r})$ denotes spatial

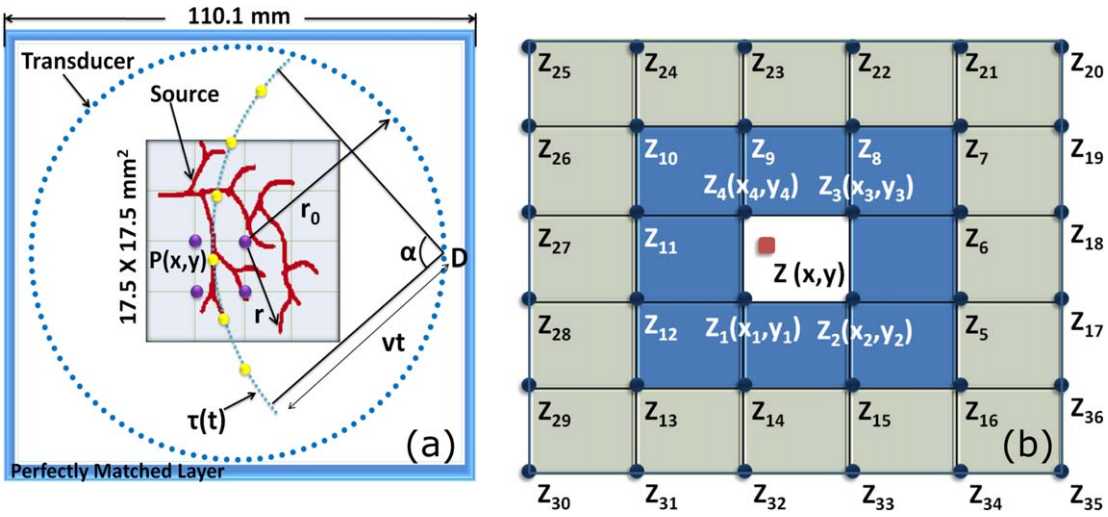

Figure 1. (a) Schematic diagram of the PAT imaging system. The PA waves originating from points (yellow dots) lying on the arc, inside the source meet at the same time at the detector (D). (b) Neighboring grid points contribute to the interpolation schemes (for BL- points inside the innermost box, for BC- points inside the middle box, for BQ- points inside the outermost box).

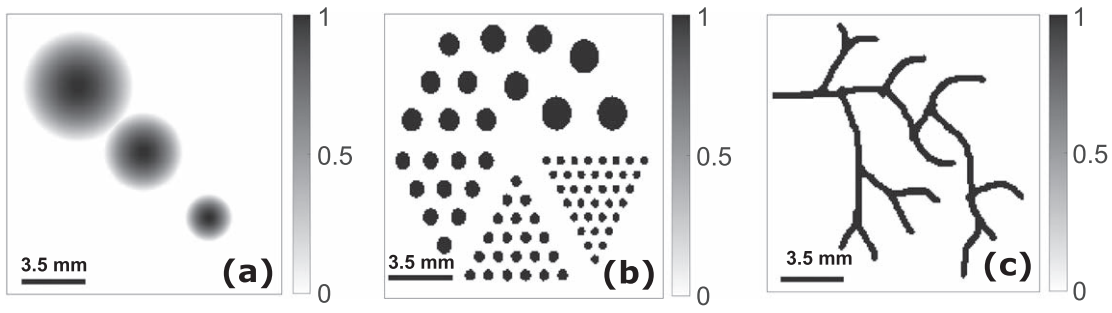

Figure 2. Numerical phantoms considered in this study- (a) Gaussian discs phantom, (b) Derenzo phantom, and (c) vasculature phantom.

distribution of light absorption and F is the fluence of the incident light beam. The solution of equation (8) in two dimensions can be given by the Poison-type integral as [11],

$$p_f(\mathbf{r}_0, t) = \frac{1}{4\pi v}\frac{\partial}{\partial t}\int_{\tau(t)} \frac{p_0(\mathbf{r})}{|\mathbf{r}_0 - \mathbf{r}|} d\tau(t), \qquad (9)$$

where $\tau(t)$ is the arc length within the illuminated region for which $|\mathbf{r}_0 - \mathbf{r}| = vt$ with $\mathbf{r}$ and $\mathbf{r}_0$ as the source and field points, respectively. The corresponding schematic diagram is shown in figure 1(a). Equation (9) states that signals from the points lying on this arc are added up coherently at $\mathbf{r}_0$ and the time derivative of the resultant signal gives rise to the PA pressure at $\mathbf{r}_0$ at time t. Equation (9) can be discretized providing [11],

$$p_f(\mathbf{r}_0, t) \approx \frac{I_{\text{abs}}(t + \Delta t) - I_{\text{abs}}(t - \Delta t)}{2\Delta t}, \qquad (10)$$

with $I_{\text{abs}}(t) = \int_{\tau(t)} \frac{p_0(\mathbf{r})}{|\mathbf{r}_0 - \mathbf{r}|} d\tau(t)$. This simple forward model explicitly asserts that the points lying on two arcs indeed participate in producing the PA pressure at $\mathbf{r}_0$ at time t. For the first arc, $|\mathbf{r}_0 - \mathbf{r}| = v(t + \Delta t)$ and for the second one, it is $v(t - \Delta t)$.

2.3. Interpolation schemes

Consider that pressure (z) at a point (x, y) needs to be estimated when those of the adjacent neighbors are known as shown in figure 1(b). In this case, simple interpolation methods can be used such as,

$$z(x, y) = \begin{cases} \sum_{k=1}^{4} W_k^{\text{BL}} z_k, & \text{for BL interpolation} \\ \sum_{k=1}^{16} W_k^{\text{BC}} z_k, & \text{for BC interpolation} \\ \sum_{k=1}^{36} W_k^{\text{BQ}} z_k. & \text{for BQ interpolation} \end{cases} \qquad (11)$$

where W_ks are the weight factors and z_ks are the pressure values at the grid crossings as shown in figure 1(b). It is clear from equation (11) that weighted contributions from 4, 16, and 36 neighboring points are considered in the case of BL, BC, and BQ interpolation schemes, respectively. Note that distal points also contribute to the estimation for the case of higher-order interpolation algorithms. The weight factors for the BL method can be presented in the

Table 1. Algorithm for calculation of interpolation coefficients. Here, $N = 4$, 16 and 36 for BL, BC and BQ, respectively.

Input:	$x, y, dx, N; x_k$s, y_ks, z_ks, $k = 1$ to N;
Output:	Interpolation weights- $W_1, W_2, ..., W_N$
Step 1:	$M \leftarrow \sqrt{N} - 1$
	Polynomial model for interpolation— $z = \sum_{i=0}^{M}\sum_{j=0}^{M} a_{ij}\left(\frac{x-x_1}{dx}\right)^i\left(\frac{y-y_1}{dy}\right)^j$
Step 2:	**for** l = 1 to M do step I
I.	Calculate z_ls using the above expansion
Step 3:	Form a system of linear equations, $z=Ba$
Step 4:	Calculate B^{-1}
Step 5:	Obtain the elements of a from, $a = B^{-1}z$
Step 6:	Determine $\Xi^T = [1, \Delta_y, ..., \Delta_y^M, \Delta_x, ..., \Delta_x\Delta_y^M, \Delta_x^2, ..., \Delta_x^2\Delta_y^M, ..., \Delta_x^M\Delta_y^M]$
Step 6:	Compute Ws using, $W = (B^{-1})^T\Xi$

following matrix form,

$$\begin{bmatrix} W_1^{\mathrm{BL}} \\ W_2^{\mathrm{BL}} \\ W_3^{\mathrm{BL}} \\ W_4^{\mathrm{BL}} \end{bmatrix} = \begin{bmatrix} 1 & -1 & -1 & 1 \\ 0 & 0 & 1 & -1 \\ 0 & 0 & 0 & 1 \\ 0 & 1 & 0 & -1 \end{bmatrix} \begin{bmatrix} 1 \\ \Delta_y \\ \Delta_x \\ \Delta_x\Delta_y \end{bmatrix} \quad (12)$$

where $\Delta_x = (x - x_1)/dx$, $\Delta_y = (y - y_1)/dy$ with $dx = dy$ is the grid size. The algorithm for determining the weight factors for each interpolation technique is presented in table 1. Equation (11) states that pressure at an internal point can be computed using the pressure data from the surrounding points. However, for the PAT image reconstruction, the inverse situation is encountered. It means that pressure data at various internal points are known but those of the grid points are not known, which can be estimated as described here.

Following the acoustic reciprocity theorem, one can distribute measured pressure (recorded at a detector at a particular instant) equally at the points lying on a specific arc [see figure 1(a)]. Therefore, pressure values at the points on the arc are known and each of them can help to estimate pressure data on the neighboring imaging grid points via an interpolation model. This forms the basis of the construction of the model matrix using interpolation methods. Thus, the relation between measured data and estimated pressure at various grid crossings can be expanded as [11],

$$p_f(\mathbf{r}_0, t_j) = \sum_{i=1}^{n} W_{ji} z_i, \quad (13)$$

where pressure is measured at t_jth instant, W_{ji} is the coefficient as shown in equation (11) and i indicates the grid number (counted by traversing the imaging region column-wise starting from the top row leftmost corner). Note that coefficients become positive for the grid crossings enclosing points on the arc for which $|\mathbf{r}_0 - \mathbf{r}| = v(t_j + \Delta t)$; however, coefficients for the grid crossings corresponding to the other arc for which $|\mathbf{r}_0 - \mathbf{r}| = v(t_j - \Delta t)$ become negative [see equation (10)]. The coefficients become zero for grid crossings that do not bound the arcs. Thus, the Λ matrix can be constructed by deploying equation (13) for all the detectors. The BL, BC, and BQ interpolation protocols have been employed in this work for image reconstruction. The same has also been done for the NN method.

3. Computational and experimental methods

3.1. Computational methods

3.1.1. Forward data simulation

The forward pressure data were simulated using k-Wave toolbox [12]. A schematic diagram of the simulation setup is presented in figure 1(a). The computational region was discretized into 1101×1101 grid points with a resolution of $dx = dy = 0.1$ mm. An absorbing layer consisting of 10 grid points was placed at each boundary. The size of the imaging region was 175×175 grid points. The density and speed of sound throughout the medium (acoustically lossless) were chosen as 1000 kg m^{-3} and 1500 m/s, respectively. In this study, 100 point detectors were positioned uniformly at a distance of 50 mm from the scanning/imaging center, covering an angular range of 0 to 2π. The center frequency of each detector was set to 2.25 MHz with 70% bandwidth. A 40 dB noise level was also added with the recorded PA signals. The sampling interval was $\Delta t = 20$ ns and the PA pressure values at 826 time points (from $1254\Delta t$ to $2079\Delta t$) for each sensor were utilized for image reconstruction. Three numerical phantoms were considered in this study, such as Gaussian discs, Derenzo, and vasculature phantoms [see figure 2]. The first phantom is composed of large absorbing regions. The PA sources are distributed all over the imaging region in the second phantom. The light-absorbing branches are thin and sharp for the third phantom.

3.1.2. Image formation

The size of the Λ matrix became $m = 57820$ and $n = 30625$. The Λ matrix was constructed in the following manner. At first, it was initialized with zeros. After that, an arc for a particular detector corresponding to a specific time point was considered [see figure 1(a)]. The entire arc length within the angle α was divided into 200 sub angles providing 201 discrete points on the arc. The next step was to find out the neighboring grid crossings (1 for NN, 4 for BL, 16 for BC, and 36 for BQ) with respect to each point lying on the arc, inside the imaging region. The corresponding interpolation weights were computed using algorithm

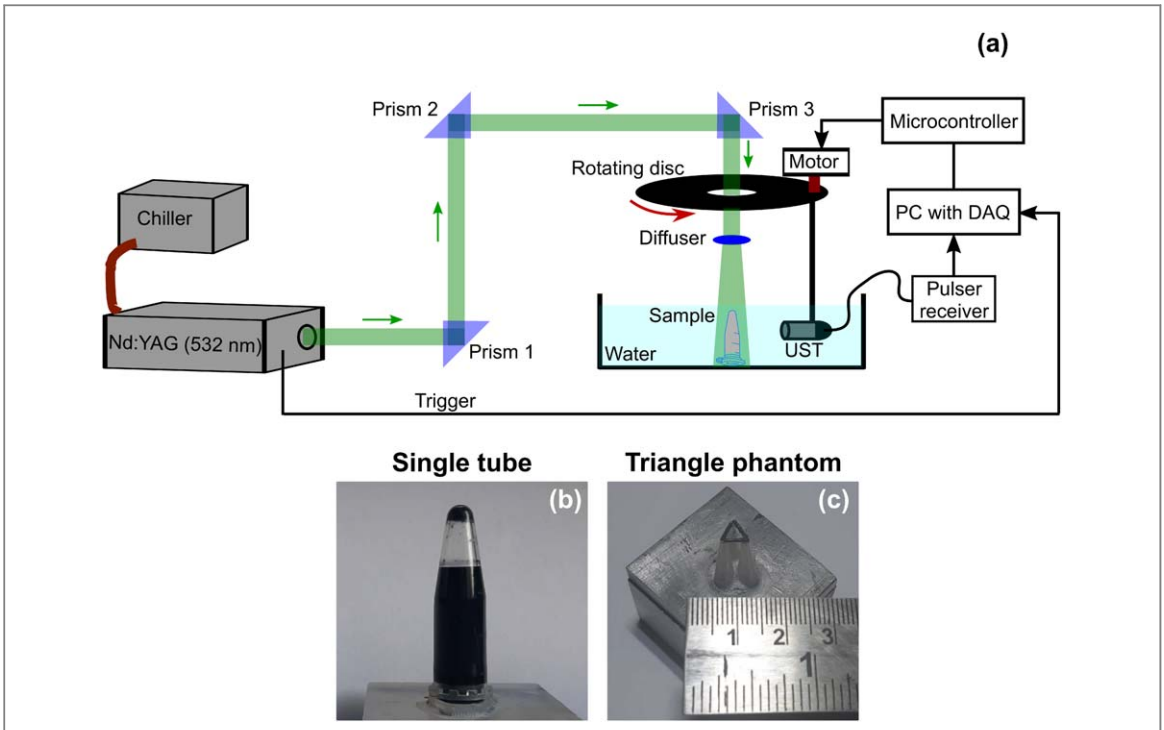

Figure 3. (a) Block diagram of the experimental setup; (b) and (c) photographs of the phantoms.

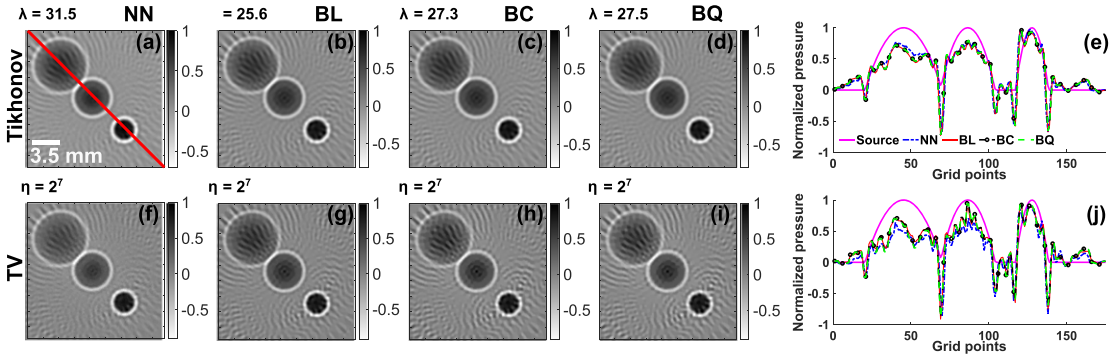

Figure 4. (a)–(d) Reconstructed images of the Gaussian discs phantom using the Tikhonov regularization method for the NN, BL, BC, and BQ protocols, respectively. (e) Plot of the PA pressure along the diagonal line as shown in each figure (green line). The same line of the source phantom is also included here for comparison. (f)–(j) Same as (a)–(e) but for the TV minimization technique.

1. The detector and time indices together provided the row location and grid crossing (its row and column indices) facilitated the column index of the Λ matrix. Therefore, a particular location in the Λ matrix was identified for each weight factor and its numerical value was added with the existing value of the Λ matrix. In this way, weight factors for all the points on the arc were loaded into the Λ matrix. The above procedure was repeated for all the time points and for all the detectors in order to form the Λ matrix. The L matrix of size $n \times n$ was formed by implementing a spatial Laplacian filter with a kernel (K_L),

$$K_L = \frac{1}{9}\begin{pmatrix} -1 & -1 & -1 \\ -1 & 8 & -1 \\ -1 & -1 & -1 \end{pmatrix}. \quad (14)$$

After building Λ and L, image reconstruction was performed using the regularization methods considered in this work. The cgsvd, l_curve, and tikhonov functions of the Regularization toolbox were used for the first approach. The cgsvd function computed the SVD of the pair of matrices (Λ, L). The l_curve function provided the optimal value of λ based on the inputs U, S and p_f. The optimized values of λ were not the same for different numerical phantoms (since the long vectors p_f were different for different phantoms). The matrices U, S, V, p_f and the optimum λ were given as the inputs for the tikhonov function, which determined the regularized solution for each phantom. The TVAL3 function (TV/L2) of the TVAL3 toolbox was employed for the second method [8, 10]. Various values of η were tried on a test image. The

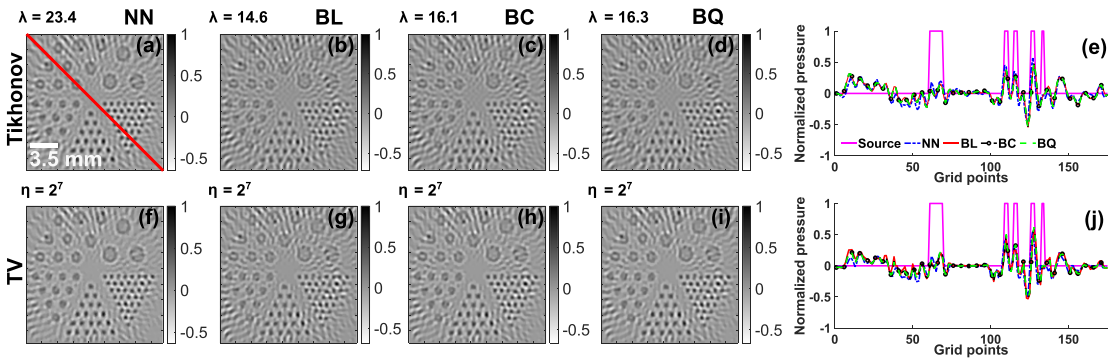

Figure 5. Same as figure 4 but for the Derenzo phantom.

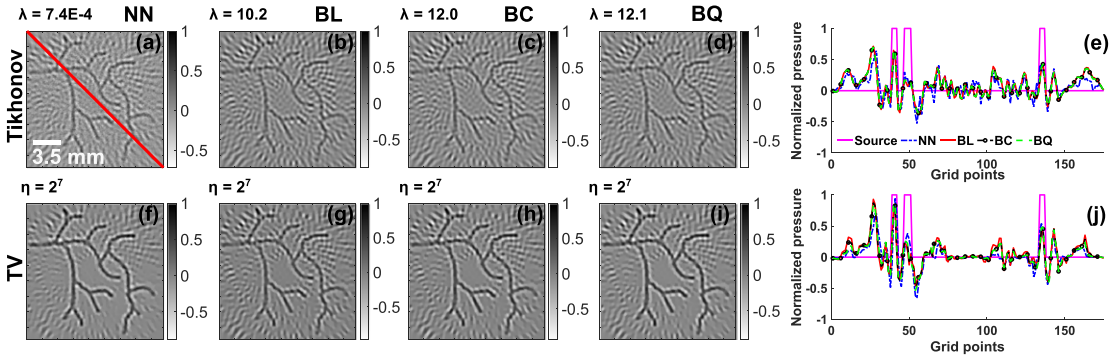

Figure 6. Same as figure 4 but for the vasculature phantom.

numerical value of η, which gave the best-reconstructed image, was utilized for this work. The numerical codes were executed in a virtual machine [CentOS, Intel Core Processor (Broadwell, IBRS) working at 2.19 GHz, 256 GB RAM, 80 Cores].

3.1.3. Computation of image quality metrics

The metrics utilized in this study are briefly described here. These metrics were calculated only for the images generated using simulated (k-Wave) PA signals.

Root mean square error (RMSE): The formula for RMSE is,

$$\mathrm{RMSE} = \sqrt{\frac{1}{n}\sum_{i=1}^{n}(z_{ti} - z_{ri})^2}, \tag{15}$$

where z_t and z_r are the initial pressure distribution in the target and the reconstructed images, respectively; both the images contain n number of pixels and the subscript i represents the ith pixel. Lower is the value of RMSE, better is the reconstruction.

Pearson's correlation coefficient (PCC): The PCC for each reconstructed image was calculated with respect to the target as [13],

$$\mathrm{PCC} = \frac{\mathrm{COV}(z_t, z_r)}{\sigma_{z_t}\sigma_{z_r}}. \tag{16}$$

The COV stands for covariance and σ indicates the standard deviation. PCC varies from –1 to 1. It approaches 1 for perfect image reconstruction.

Contrast to noise ratio (CNR): The formula for calculating the CNR is given by [14],

$$\mathrm{CNR} = \frac{\mu_{roi} - \mu_{back}}{(\sigma_{roi}^2 n_{roi} + \sigma_{back}^2 n_{back})^{\frac{1}{2}}}, \tag{17}$$

where, 'roi' and 'back' are the source and the background regions of the reconstructed image. Here, μ represents the mean; $n_{roi} = A_{roi}/A_{total}$ and $n_{back} = A_{back}/A_{total}$ where A_{roi} and A_{back} are the total number of pixels in the ground truth with $p_0 \neq 0$ and $p_0 = 0$, respectively; A_{total} is the total number of pixels in the original/reconstructed image.

Structure similarity index measure (SSIM): The SSIM quantifies the structural similarity between the target and the reconstructed image. The SSIM can be determined by evaluating the following equation [15],

$$\mathrm{SSIM} = \frac{(2\mu_{z_t}\mu_{z_r} + c_1)(2\ \mathrm{COV}(z_t, z_r) + c_2)}{(\mu_{z_t}^2 + \mu_{z_r}^2 + c_1)(\sigma_{z_t}^2 + \sigma_{z_r}^2 + c_2)}. \tag{18}$$

In case of weak denominator, c_1 and c_2 stabilize the above equation. The SSIM can be computed using the inbuilt ssim function of Matlab, which, by default, assigns the numerical values of c_1 and c_2. The pressure values associated with pixels for both the target and the reconstructed images were mapped (using shifting and scaling), with respect to the same scale ranging from 0 to 1, into 256 gray levels. After that SSIM was calculated for each interpolation scheme.

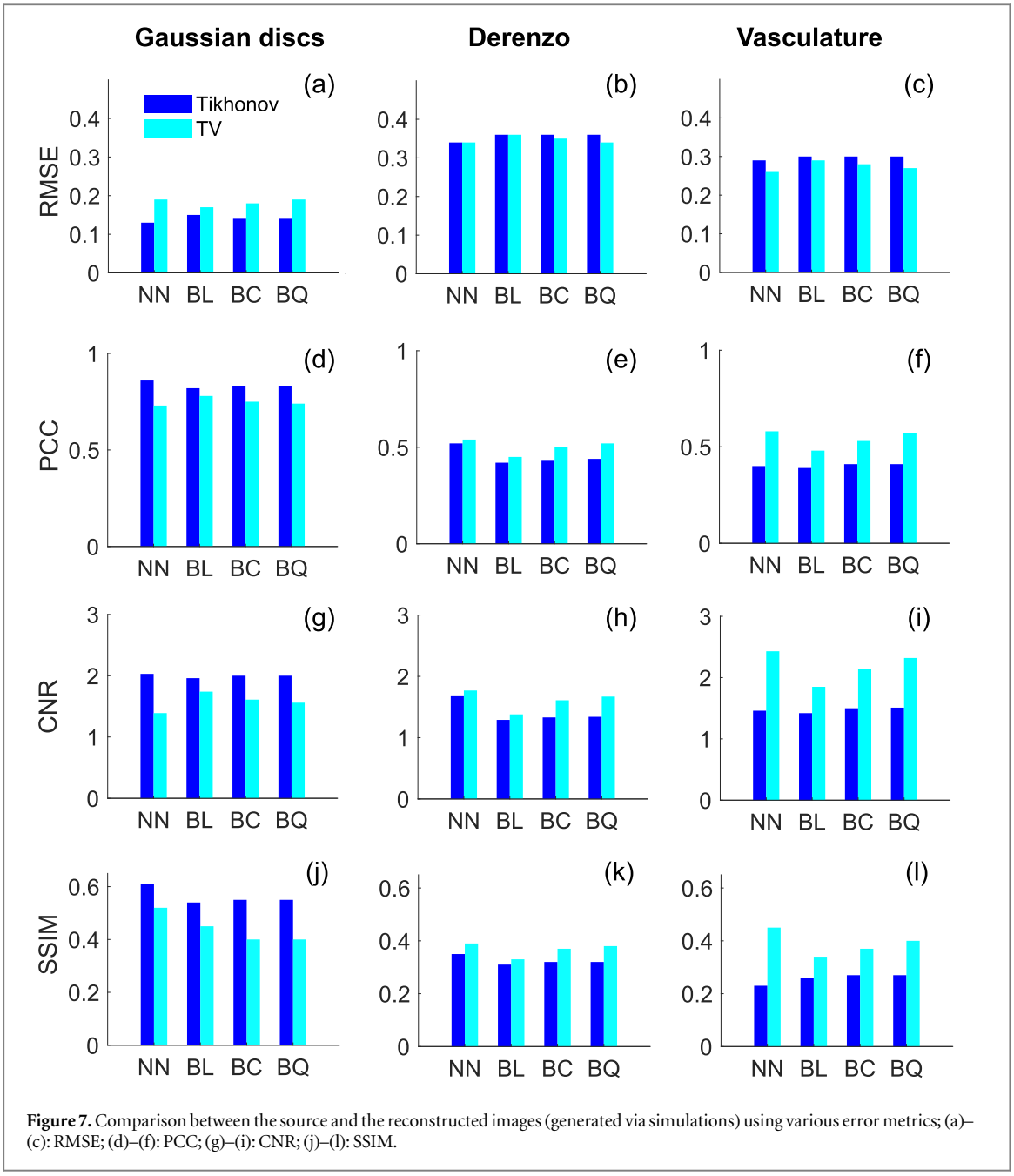

Figure 7. Comparison between the source and the reconstructed images (generated via simulations) using various error metrics; (a)–(c): RMSE; (d)–(f): PCC; (g)–(i): CNR; (j)–(l): SSIM.

3.2. Experimental procedure

The details of the experimental setup is displayed in figure 3(a). A Q-switched, Nd:YAG, nanosecond, pulsed laser (NT352C-10-SH-H, Ekspla) was deployed to emit a 532 nm beam with 6 ns pulse duration at 10 Hz repetition rate (energy per pulse was nearly 13.7 mJ cm^{-2}). A single-element ultrasonic detector (V325-SU, Panametric) with 2.25 MHz, 70% and 9.5 mm as the center frequency, fractional bandwidth, and diameter, respectively captured the PA signals. The detected signals were preprocessed using a pulser/receiver (DPR300, JSR Ultrasonics). Such signals were digitized (25 MHz as the sampling frequency) and stored using a data acquisition card (PCIe-9852, ADLINK). The transducer revolved around the sample in a circular path covering 360 degrees (scanning radius was about 47 mm). The scanning speed was set to 0.5 degree/s. A customized setup was built for this purpose (Holmarc, India). The PA pressure data were collected from two phantoms as shown in figures 3(b) and (c). A plastic tube was filled with black ink in the case of the first phantom. A triangular shape was constructed using pencil leads (Graphite) in the case of the second phantom. The radio frequency lines for 100 detector locations (signal at each location was obtained by taking the average from 20 lines) were utilized for image reconstruction. The size of the reconstructed image became 101 × 101 pixels with $dx = dy = 0.2$ mm. To compare the performance of the interpolation methods, signal-to-noise ratio (SNR) was computed for each reconstructed image. The SNR is defined as,

$$\mathrm{SNR} = 20\log_{10}\left(\frac{A}{\sigma_{back}}\right), \tag{19}$$

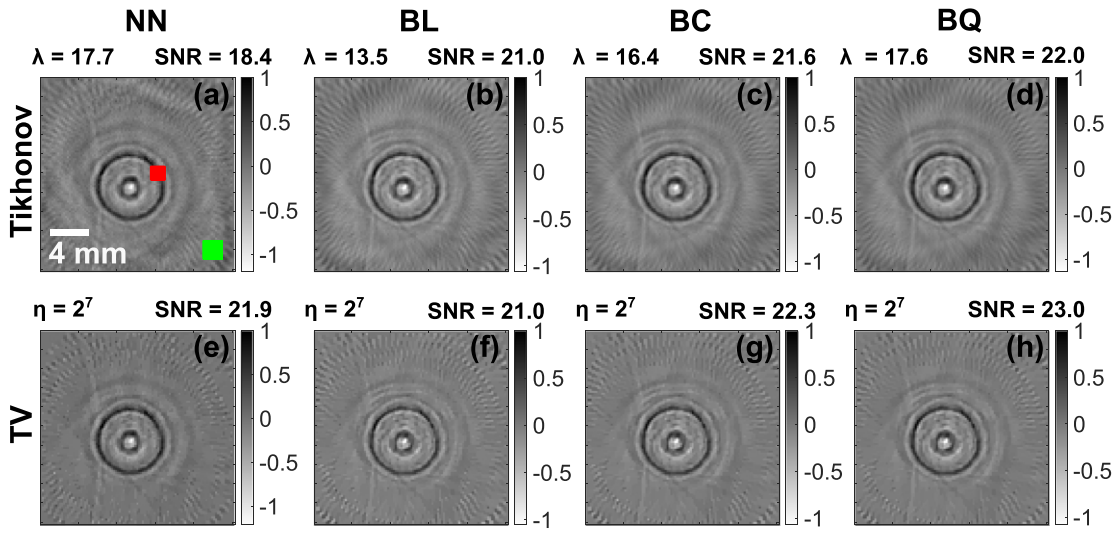

Figure 8. Image formation using the experimental data recorded for the single tube phantom. The penalty parameters (λ, η) are given in the respective images. The signal-to-noise ratio (SNR) for each image is pasted at the top right corner. The unit of SNR is dB.

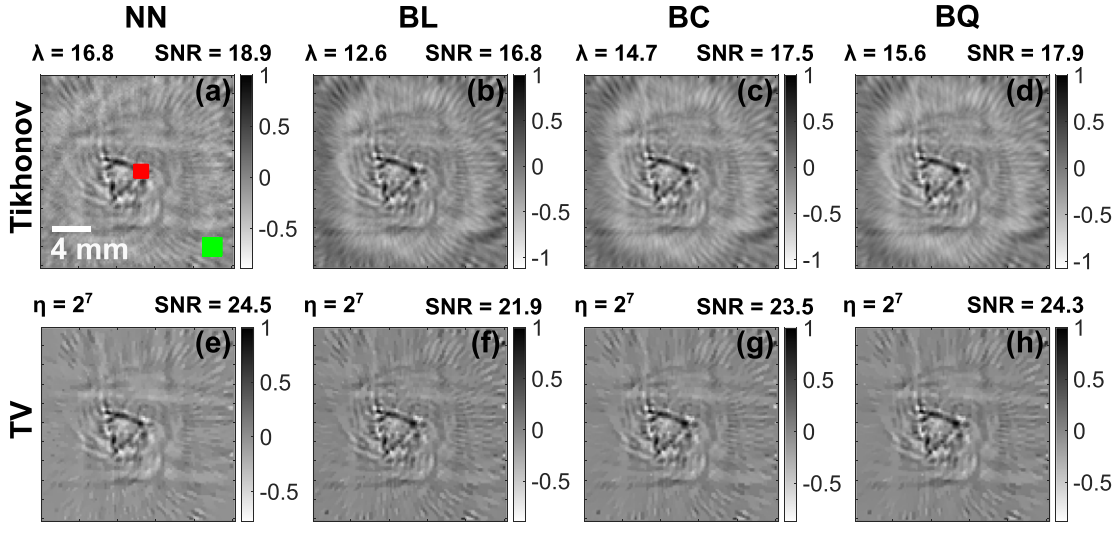

Figure 9. Image reconstruction of the triangular phantom utilizing measured signals (same as figure 8).

where A is the peak pressure value in 'roi' and σ_{back} represents the standard deviation of 'back'. The pressure values at the red (region of interest- 64 pixels) and the green (background region- 121 pixels) sectors have been utilized to calculate the SNR [see figure 8(a)].

4. Image reconstruction results

4.1. Computational results

Figures 4(a)–(d) display the reconstructed images of the multiple Gaussian discs phantom generated by the Tikhonov regularization method for the NN, BL, BC, and BQ protocols, respectively. The plot of the PA pressure along the diagonal line of each image is shown in figure 4(e). The same quantity for the source phantom is also included in this figure for comparison. The corresponding images obtained from the TV minimization method are presented in figures 4(f)–(j). The images constructed by various methods are pretty similar and no significant difference can be seen. This is consistent with the line plots [figures 4(e) and (j)] and figure 7. For example, the numerical values of RMSE, PCC, and CNR are comparable for the NN, BL, BC, and BQ methods in each regularization framework [see figure 7(a), (d) and (g), respectively]. However, the SSIM for the NN technique is slightly higher than those of the other schemes [see figure 7(j); approximately 13% higher with respect to the BL for the Tikhonov method].

Simulated images of the Derenzo and vasculature phantoms are shown in figures 5 and 6, respectively. Note that all the methods can recover the small structures much more accurately than the large discs

Table 2. Chart displaying execution time taken for image reconstruction by each method.

Phantom	Tikhonov (s)				TV (s)			
	NN	BL	BC	BQ	NN	BL	BC	BQ
SVD	4572	4755	4212	3946				
Gaussian discs	30	33	32	32	508	415	450	567
Derenzo	30	31	33	32	590	460	490	619
Vasculature	30	31	31	32	583	483	512	613

present within the illuminated region and they perform quite equally (see figure 5). The image quality metrics generally do not vary significantly for this phantom (second column of figure 7). In the case of the vasculature phantom, the NN algorithm along with the TV framework works much better than the other approaches (compare figure 6(f) with others). It is clear from the third column of figure 7 that each metric corresponding to the NN algorithm is either comparable or higher than that of the higher-order protocols. For instance, CNR attains the highest value for the TV formulation (see figure 7(i)).

4.2. Experimental results

The reconstructed images of the experimental phantoms are presented in figures 8 and 9. The optimum value of λ for each interpolation method is pasted at the top left corner of each figure. The numerical value of SNR computed for each image is also given at the top right corner. It is clear from figure 8 that improved imaging is possible if one uses higher-order interpolation methods instead of the NN scheme. In particular, the region outside the tube has been reproduced in a much better fashion in figures 8(b)-(d) than that of figure 8(a). This is also true for the TV method (see bottom row of figure 8). Moreover, SNR values in general gradually increase as the complexity of interpolation increases. Similar figures for the triangular phantom are shown figure 9. The NN protocol appears to be the best method and this can be observed for both the regularization methods. As in the previous case, noise cleaning at the distal regions (from the center) is better in the TV technique in comparison to the Tikhonov technique.

5. Discussion and conclusions

In this work, we utilized various interpolation schemes for constructing the system matrix. Note that pressure at an interpolating point depends upon its magnitude at the nearest grid crossing in the NN model whereas grid crossings at distal regions also contribute in higher-order models. It may be thought of as a diffusion process, which may work favourably for the reconstruction of large objects. This is not distinctly clear from the simulation results (see figure 4) but is evident from the experimental results (see figure 8). That is why the SNR values for the BL, BC, and BQ methods are higher than that of the NN method for the single tube phantom. The diffusion process may introduce redundant and wrong information for a PA source with thin and sharp branches (e.g., blood vessels). This may be the reason for which higher-order models formed relatively low-quality images than that of the NN model for the vasculature phantoms (see figure 6 and figure 9). It would be interesting in the future to evaluate the performance of these interpolation methods for PAT imaging with finite sensors. Additionally, the efficacy of B-spline and other interpolation techniques may also need to be investigated.

One of the important aspects of the Tikhonov regularization is to find out the optimum regularization parameter (λ). Various methods have been tested to accomplish this [16, 17]. In these works, the system matrix was built using the time domain signals generated by the individual pixels and recorded by each detector. Previously, we also constructed the system matrix in this manner [13] and the L-curve technique was employed to determine the optimized λ. Its numerical value demonstrated a good correlation with the literature. Nevertheless, the numerical values of λ evaluated in this work were in general found to be on the higher side with respect to those of the literature [13, 16, 17]. Note that the system matrix in an interpolation method is built based on the distances of the grid points from the individual points with known PA pressure. Therefore, it is a different procedure than the impulse response-based method. This may be the reason for which the numerical values of λ in this work were computed to be greater than the reported values. However, additional work is needed to resolve this issue. We also plan to employ the impulse response-based method for the generation of the system matrix and perform image reconstruction using measured signals.

This paper includes l_2 norm-based Tikhonov and l_1 norm-based TV regularizations for PA image reconstruction. The first method took a longer time to execute than the second algorithm. The computational time for various techniques is detailed in table 2. It illustrates that the computational time decreases for the Tikhonov technique (see row 3, columns 3-5 of table 2) and increases for the TV method (see rows 4-5,

columns 7-9 of table 2) as the order of the interpolation scheme increases. It may be mentioned here that the execution time presented herein is significantly higher than the values reported in the literature [18]. Awasthi *et al* performed the TV regularization using a toolbox that implements split augmented Lagrangian shrinkage algorithm (SALSA) whereas the ALADA algorithm is realized in the TVAL3 toolbox. Afonso *et al* originally implemented the SALSA algorithm in the context of image processing [19]. It seems that the SALSA algorithm works faster than the ALADA protocol. Further investigation is required to address the same issue for the Tikhonov regularization technique. It may also be emphasized here that recently fractional regularization techniques [9] have been applied for PAT imaging. It has been shown that fractional methods can provide improved image reconstruction. Therefore, it would also be interesting to implement fractional techniques for tomography imaging.

In conclusion, the reconstructed images for an extended light absorbing object look similar for all the interpolation methods (i.e., NN, BL, BC, BQ). It is true for both the minimization procedures. The NN algorithm in combination with the TV minimization protocol provides acceptable reconstructed images for a PA source containing several thin and sharp branches. The simplest NN scheme emerges as the most suitable candidate for vascular imaging in practice.

Acknowledgments

The computational results reported in this work were performed on the Central Computing Facility of IIITA, Allahabad. This work was supported by the ICMR grant (# 56/2/2020-Hae/BMS).

Data availability statement

No new data were created or analysed in this study.

Disclosures

The authors declare no conflicts of interest.

ORCID iDs

Ratan K Saha https://orcid.org/0000-0001-7274-6707

References

[1] Wang L V and Yao J 2016 A practical guide to photoacoustic tomography in the life sciences *Nat. Methods* **13** 627–38
[2] Attia A B E, Balasundaram G, Moothancherya M, Dinisha U S, Bia R, Ntziachristos V and Olivoa M 2019 A review of clinical photoacoustic imaging: Current and future trends *Photoacoustics* **16** 100144
[3] Wang L V 2009 *Photoacoustic Imaging and Spectroscopy* (Boca Raton, FL: CRC Press) 37–46 Chap. 4
[4] Warbal P, Pramanik M and Saha R K 2019 Impact of sensor apodization on the tangential resolution in photoacoustic tomography *J. Opt. Soc. Am.* A **36** 245–52
[5] Shaw C B, Prakash J, Pramanik M and Yalavarthy P K 2013 Least square QR-based decomposition provides an efficient way of computing optimal regularization parameter in photoacoustic tomography *J. Biomed. Opt.* **18** 080501
[6] Déan-Ben X L, Ntziachristos V and Razansky D 2012 Accurate model-based reconstruction algorithm for three-dimensional optoacoustic tomography *IEEE Trans. Med. Imag.* **31** 1922–8
[7] Lehmann T M, Gonner C and Spitzer K 1999 Survey: Interpolation methods in medical image processing *IEEE Trans. Med. Imag.* **18** 1049–75
[8] Hansen P C 2007 Regularization Tools Version 4.0 for Matlab 7.3 *Numer. Algorithms* **46** 189–94
[9] Prakash J, Sanny D, Kalva S K, Pramanik M and Yalavarthy P K 2019 Fractional regularization to improve photoacoustic tomographic image reconstruction *IEEE Trans. Med. Imaging* **38** 1935–47
[10] Li C, Yin W, Jiang H and Zhang Y 2013 An efficient augmented Lagrangian method with applications to total variation minimization *Comput. Optim. Appl.* **56** 507–30
[11] Déan-Ben X L, Ntziachristos V and Razansky D 2012 Acceleration of optoacoustic model-based reconstruction using angular image discretization *IEEE Trans. Med. Imag.* **31** 1154–62
[12] Treeby B E and Cox B T 2010 k-wave: MATLAB toolbox for the simulation and reconstruction of photoacoustic wave fields *J. Biomed. Opt.* **15** 021314
[13] Prakash R, Badal D, Paul A, Sonker D and Saha R K 2021 Photoacoustic signal simulation using discrete particle approach and its application in tomography *IEEE Trans. Ultrason. Ferroelectr. Freq. Control* **68** 707–17
[14] Song X, Pogue B W, Jiang S, Doyley M M, Dehghani H, Tosteson T D and Paulsen K D 2004 Automated region detection based on the contrast-to-noise ratio in near-infrared tomography *Appl. Opt.* **43** 1053–62
[15] Wang Z, Bovik A C, Sheikh H R and Simoncelli E P 2004 Image quality assessment: from error visibility to structural similarity *IEEE Trans. Image Process.* **13** 600–12
[16] Bhatt M, Acharya A and Yalavarthy P K 2016 Computationally efficient error estimate for evaluation of regularization in photoacoustic tomography *J. Biomed. Opt.* **21** 106002
[17] Bhatt M, Gutta S and Yalavarthy P K 2016 Exponential filtering of singular values improves photoacoustic image reconstruction *J Opt. Soc. Am A* **33** 1785–92
[18] Awasthi N, Kalva S K, Pramanik M and Yalavarthy P K 2018 Image-guided filtering for improving photoacoustic tomographic image reconstruction *J. Biomed. Opt.* **23** 091413
[19] Afonso M V, Bioucas-Dias J M and Figueiredo M A T 2010 Fast image recovery using variable splitting and constrained optimization *IEEE Trans. Image Process* **19** 2345–56